Electromagnetically induced transparency based Rydberg-atom sensor for traceable voltage measurements (F)

(iD) Christopher L. Holloway, (iD) Nikunjkumar Prajapati, Jeffery A. Sherman, et al.

COLLECTIONS

Paper published as part of the special topic on Quantum Sensing as a Technology

(F) This paper was selected as Featured

View Online

Export Citation

ARTICLES YOU MAY BE INTERESTED IN

Determining the angle-of-arrival of a radio-frequency source with a Rydberg atom-based sensor
Applied Physics Letters **118**, 114001 (2021); https://doi.org/10.1063/5.0045601

Continuously tunable radio frequency electrometry with Rydberg atoms
Applied Physics Letters **121**, 014002 (2022); https://doi.org/10.1063/5.0086357

Enhancement of electromagnetically induced transparency based Rydberg-atom electrometry through population repumping
Applied Physics Letters **119**, 214001 (2021); https://doi.org/10.1063/5.0069195

AVS Quantum Science

Co-Published by

AIP Publishing / AVS

RECEIVE THE LATEST UPDATES

Electromagnetically induced transparency based Rydberg-atom sensor for traceable voltage measurements ⓕ

View Online   Export Citation   CrossMark

Christopher L. Holloway,[1,a)] ⓘ Nikunjkumar Prajapati,[1] ⓘ Jeffery A. Sherman,[1] Alain Rüfenacht,[1]
Alexandra B. Artusio-Glimpse,[1] Matthew T. Simons,[1] ⓘ Amy K. Robinson,[2] ⓘ David S. La Mantia,[3,4]
and Eric B. Norrgard[3] ⓘ

AFFILIATIONS

[1]National Institute of Standards and Technology, Boulder, Colorado 80305, USA
[2]Department of Electrical Engineering, University of Colorado, Boulder, Colorado 80305, USA
[3]National Institute of Standards and Technology, Gaithersburg, Maryland 20899, USA
[4]University of Maryland, College Park, Maryland 20740, USA

Note: This paper is part of the special topic collection, Quantum Sensing as a Technology.
[a)]Electronic mail: christopher.holloway@nist.gov

ABSTRACT

We investigate the Stark shift in Rydberg rubidium atoms through electromagnetically induced transparency for the measurement of direct current (dc) and 60 Hz alternating current (ac) voltages. This technique has direct application to the calibration of voltage measurement instrumentation. We present experimental results for different atomic states that allow for dc and ac voltage measurements ranging from 0 to 12 V. While the state-of-the-art method for realizing the volt, the Josephson voltage standard, is significantly more accurate, the Rydberg atom-based method presented here has the potential to be a calibration standard with more favorable size, weight, power, and cost. We discuss the steps necessary to develop the Rydberg atom-based voltage measurement as a complementary method for dissemination of the voltage scale directly to the end user and discuss sources of uncertainties for these types of experiments.

Published by AIP Publishing. https://doi.org/10.1116/5.0097746

I. INTRODUCTION

Rydberg atoms (atoms with one or more electrons excited to a very high principal quantum number n^1) in conjunction with electromagnetically induced transparency (EIT) techniques have been used to successfully detect and fully characterize radio frequency (RF) electric (E) fields.[2–7] In these applications, the E-fields are detected using EIT both on resonance as Autler–Townes (AT) splitting and off-resonance as ac Stark shifts. This approach has the capability of measuring amplitude,[3–6,8–11] polarization,[12,13] and phase[14,15] of the RF field, and various applications are beginning to emerge.[16] These include E-field probes[5,6,10] traceable to the International System of Units (SI), power sensors,[17] spectrum analyzers,[18] angle-of-arrival detection,[19] receivers for communication signals (AM/FM modulated and digital phase modulation signals),[20–27] and even video reception.[28]

In this paper, we investigate the use of Rydberg-atom sensors to develop a quantum-based voltage standard. We measure the voltage induced between two parallel plates embedded in an atomic vapor cell

(see Fig. 1) by measuring the Stark shifts in the atomic spectra of Rydberg atoms. By collecting a series of measurements of the Stark shift for different applied voltages, we can make a calibration curve and demonstrate a voltage standard. We discuss various issues that must be considered in order for Rydberg-atom-based sensors to accurately and reliably function as voltage measurement standards.

The primary voltage standard implemented for the realization of the SI volt is based on the Josephson effect. Arrays of Josephson junctions, when cooled to cryogenic temperatures and biased on their quantum locking range, transduce an accurately synthesized microwave frequency source into fixed or digitally programmable voltages.[29] Comparisons between such voltage standards demonstrate accuracies at the level of 1 part in 10^{10} with about 100 s of averaging (see, e.g., Ref. 30). Scaling up the voltage output of Josephson-junction based standards requires either increasing the number of junctions in the array, or increasing the microwave driving frequency, or both.[31] With some exceptions (see, e.g., Ref. 32), 10 V is the commonly adopted dc
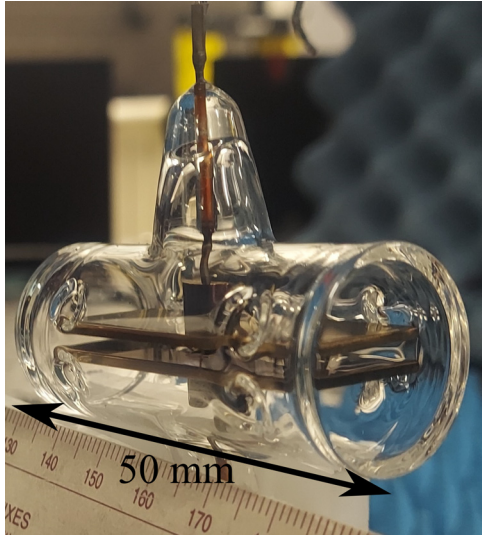
FIG. 1. Cylindrical vapor cell with stainless-steel parallel plates. The vapor cell is 50 mm in length and has an outside diameter of 25 mm. The plates are rectangular in shape with the width of 18 mm and the length of 45 mm and placed $\approx$2 mm apart.

reference for the primary realization of the voltage scale. Commercial instruments (such as voltage calibrators) used for the routine voltage calibration process and voltage dividers implemented to expand the range to high voltages typically have an accuracy on the order of 1 part in 10^6.[33] Due to their large cost ($\gtrsim$\$300 k), Josephson voltage standards limit their deployment to national metrological institutes (NMIs) or primary calibration laboratories.

Zener diodes are the most commonly used voltage references that are implemented with commercial instrumentation, ranging from high performance secondary voltage standard (>\$10k)[34,35] to the 0.1% accuracy handheld multimeters ($\approx$ \$100). All Zener-diode voltage references drift with time and require periodic calibration, which involves a comparison with a more accurate voltage reference or another verification of the manufacturer's specifications. Zener-diode references are sensitive to temperature, humidity, barometric pressure, mechanical stress and shock, and power supply noise.[34]

Rydberg atom sensors are a potential alternative to Josephson junctions and Zener diodes as a voltage standard. Atomic systems have a predictable response to an applied electric field. For example, polarizability measurements with low-lying excited states of alkaline-earth atoms show total inaccuracy at the level of two parts in 10^5.[36,37] Because the polarizability is proportional to n^7, with n is the principal quantum number, Rydberg atomic states have high sensitivity to electric fields. Furthermore, Rydberg atoms have high intrinsic response bandwidth and can be produced by laser excitation in large quantities within simple vapor cells at or near room temperature. In principle, the atomic response can be made free from environmental coupling, which would make Rydberg atom sensors intrinsically stable, eliminating the need for subsequent periodic external calibrations.

In this paper, we discuss various nuances of Rydberg-atom-based voltage measurements [e.g., the effects of energy level crossings (ELCs) and non-parallel electrodes]. While similar measurements have been performed before,[38–41] our study focuses on the aspects that will need

to be addressed and controlled for a Rydberg-atom sensor to be used as a voltage measurement standard. We also demonstrate two methods for measuring ac voltage amplitude at 60 Hz.

II. THEORY

The interaction of an atomic system with an electric field E may be described by the effective Hamiltonian,

$$H_{\text{eff}} = H_0 + H_S, \tag{1}$$

where H_0 is the field-free Hamiltonian of the atomic system, and

$$H_S = -\mu_{ij}^z E \tag{2}$$

is the Hamiltonian describing the Stark interaction. Here, μ_{ij}^z is the component of the dipole matrix element between atomic states i and j along the local electric field E. We calculate the energy eigenstates, up to the accuracy with which the dipole matrix elements are known, by diagonalizing H_{eff}. We check for convergence by increasing the basis size until we obtain convergence within the desired accuracy, typically 0.1%. By subtracting the field-free energies from the field-applied energies, we obtain the Stark shift Δ.

In this work, we use dipole matrix elements μ_{ij} taken from the Alkali Rydberg Calculator Python package.[42] This package calculates dipole matrix elements using the Coulomb approximation (CA) and the quantum defects given in Ref. 43. Reference 44 compared the accuracy of CA calculations to calculations with the more detailed Dirac–Fock with core potential approach and found an accuracy of better than 1% for the 28S to 47S Rydberg states considered here. The accuracy of the theoretical values exceeds the experimental accuracy for these states, which is typically on the level of a few percent.[47,48]

For nondegenerate state i, the Stark shift may be approximated by[50]

$$\Delta = -\frac{\alpha_i(f)}{2} E^2, \tag{3}$$

where the polarizability of state i is

$$\alpha_i(f) = \sum_j \frac{|\mu_{ij}^z|^2}{h} \left(\frac{1}{f_{ij} - f - \frac{i}{2}\Gamma_j} + \frac{1}{f_{ij} + f + \frac{i}{2}\Gamma_j} \right). \tag{4}$$

Here, E is the applied electric field (in units of V/m) with frequency f (in units of Hz) and $\alpha_i(f)$ is the polarizability [in units of Hz/(V^2/m^2)]. The summation includes all states j, which are coupled to i by an electric field, f_{ij} is the transition frequency (in units of Hz) between states i and j, and Γ_j is the spontaneous decay rate (in units of Hz) of state j. For the 28S to 47S Rydberg states considered here, $f_{ij} \gtrsim 1$ GHz $\gg$ 60 Hz; we can, therefore, apply calculations for dc electric fields to 60 Hz ac fields to a precision of <0.1%.

A Rydberg atom-based voltage measurement is performed by applying a voltage V between the parallel plates with separation d in the atomic vapor cell (see Fig. 1) to generate a uniform electric field (neglecting fringing field, see discussion in Sec. IV B),

$$E = V/d. \tag{5}$$

We then observe the induced differential Stark shift Δ in the coupling laser EIT signal. Because the Stark shift Δ is an even function of E, Δ is independent of the polarity of the applied voltage.

Although Eq. (3) is only strictly valid in the limit where $E\mu_{ij}^z \ll hf_{ij}$, it is useful for quickly estimating the Stark shift due to its quadratic scaling. Equation (3) may also be used for uncertainty estimates. Using Eq. (3), the voltage can be found by the measurement of Δ,

$$|V| = d\,\sqrt{\frac{2\,|\Delta|}{\alpha}}. \qquad (6)$$

From Eq. (6), we see that there are three parameters of interest in this measurement. There are two measured quantities in this expression (the plate separation d and the Stark shift Δ) and one calculated quantity (the atomic polarizability, α). The measurement of Δ can be related to *in situ* laser spectroscopy of the hyperfine structure, contributing to relative precision of 10^{-7} or better.[49] Relative uncertainty in d of 10^{-4} is possible with gauge-block construction[45] or at $<2 \times 10^{-5}$ with interferometric techniques.[36,37] Typically, poor knowledge of μ_{ij} limits the calculation of α to the 10^{-3} level, though in some cases, α is experimentally determinable by other means.[46] From these considerations, a voltage standard based on Rydberg atoms, which relies only on knowledge of fundamental constants, could potentially be constructed with an uncertainty of 10^{-4} or better.

Even without knowledge of the plate separation d, the quantity $d/\sqrt{|\alpha|}$ can be calibrated to the extent that d remains stable. For a given device, Eq. (6) may be recast as

$$|V| = C_{\text{cal}}\sqrt{|\Delta|}, \qquad (7)$$

where

$$C_{\text{cal}} = \sqrt{2}d/\sqrt{\alpha} \qquad (8)$$

and is determined by comparison to a higher accuracy voltage standard or by use of several Rydberg states with various α of lower uncertainty.

III. EXPERIMENTAL SETUP

In these experiments, we generate EIT in rubidium (^{85}Rb) atomic vapor and measure the frequency shift in the EIT signal (i.e., the Stark shift, Δ) as a function of an applied voltage across two parallel plates. The experimental setup and the atomic levels used are depicted in Fig. 2, which consists of a 780 nm probe laser [wavelength of $\lambda_p = 780.24$ nm (Ref. 51)], a 480 nm coupling laser ($\lambda_c \approx 480$ nm), a photodetector connected to an oscilloscope, a voltage source, a voltage meter, and the vapor cell shown in Fig. 1 filled with ^{85}Rb atomic vapor. We use a three-
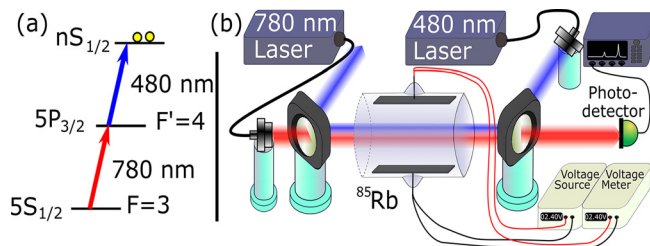
level EIT scheme to generate Rydberg atoms [see Fig. 2(a)], which corresponds to the ^{85}Rb $5S_{1/2}$ as the ground state, $5P_{3/2}$ as the intermediate state, and a Rydberg state of the n $S_{1/2}$ state. In our experiments, we use $n = 47$, $n = 40$, and $n = 28$ (corresponding to $\lambda_c = 483.166$, 480.919, and 480.371 nm, respectively). The probe laser is locked to the D2 transition $[5S_{1/2}(F = 3)\text{–}5P_{3/2}(F = 4)]$ and to produce an EIT signal, we apply a counter-propagating coupling laser scanned across the $5P_{3/2}\text{–}nS_{1/2}$ Rydberg transition. We modulate the coupling laser amplitude with a 37 kHz square wave and use a lock-in amplifier to isolate the EIT signal from the Doppler background.

While we focus on nS Rydberg levels in this work, we note that it is possible to perform measurements in nD Rydberg levels with this setup as well. However, the Stark spectrum of nD levels is complicated by the presence of fine structure and tensor polarizability contributions, and many more states with similar energy (Fig. 3). However, as we will see below, for large applied voltages, the S-state spectra can be influenced by nearby state energies as well.

We use a custom cylindrical Rb vapor cell of length 50 mm and diameter of 25 mm, Fig. 1. Inside the cell are two stainless-steel parallel plates with a nominal separation of $d = 2$ mm. A voltage source is connected to the electrodes on the outside of the vapor cell. These electrodes penetrate the cell and are connected to the two parallel plates. The voltage sources and the voltage meter were calibrated before the experiments and the absolute voltage accuracy of any reading is 0.5 mV. In these experiments, the optical beams and the electric fields between the two plates are co-linearly polarized. The probe laser was focused to a full-width at half maximum (FWHM) of 80 μm with a power of 3.6 μW, and the coupling laser was focused to a FWHM of 110 μm with a power of 70 mW. We then observe the induced differential Stark shift Δ in the EIT signal as the coupling laser is scanned.

Table I gives the calculated dc polarizability $\alpha(0)$ for the atomic states used here using Eq. (4) and dipole matrix elements μ_{ij} taken from the Alkali Rydberg Calculator Python package.[42] As the polarizability of the $5P_{3/2}$ state is smaller than that of the $nS_{1/2}$ Rydberg state by at least 3 orders of magnitude, the observed differential Stark shift may be taken to be simply the Stark shift of the Rydberg state within the precision of this work. The Stark shift of the $5P_{3/2}$ state may be

FIG. 2. (a) Level diagram depicting EIT coupling the $5S_{1/2}(F = 3)$ state to an $nS_{1/2}(F = 3)$ Rydberg state through the $5P_{3/2}(F = 4)$ intermediate state. (b) Experimental setup for the voltage measurement and the three-level EIT scheme.
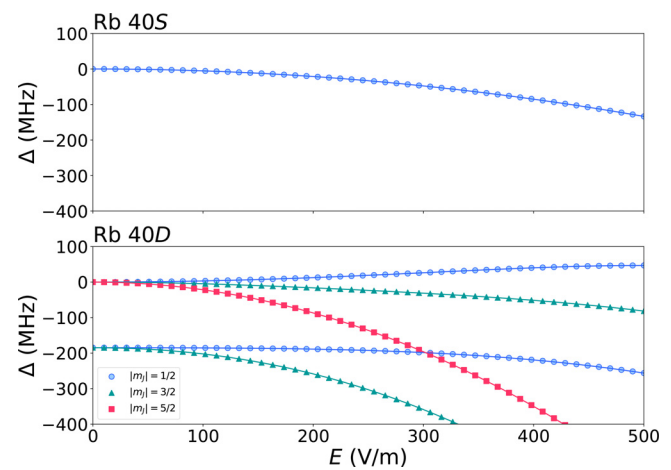
FIG. 3. Calculated dc Stark shift Δ in Rb as a function of electric field E for 40S and 40D.

TABLE I. Theoretical calculation of dc and 60 Hz ac polarizabilities for ^{85}Rb. Note that the dc and 60 Hz ac polarizabilities are essentially the same for the digits shown.

Calculated polarizability [Hz/(V/m)^2]	
Rydberg state	α: dc and 60 Hz ac
$28S_{1/2}$	84.2
$40S_{1/2}$	1058.1
$47S_{1/2}$	3275.7

calculated by the same methods in cases where increased theoretical precision is required. We note that the ground state polarizability of alkalis may be measured to roughly 0.2% uncertainty using interferometric techniques.[46]

IV. EXPERIMENTAL DATA

In this section, we detail general observations of the Rydberg atom-based voltage measurement. A description of systematic errors and uncertainties follows in Sec. V.

The EIT signals for two different applied voltages are shown in Fig. 4(a). These results are for the $40 S_{1/2}$ state as the coupling laser is scanned. To increase the signal-to-noise ratio, we gather 20 oscilloscope traces and average them after accounting for laser drift using an external reference EIT signal. The two different traces correspond to the zero voltage case (black-solid trace) and the case with -2.4 V applied (red-dashed trace). When a voltage is applied, the EIT peak shifts by Δ according to Eq. (6); e.g., applying -2.4 V shifts the EIT peak to around -850 MHz (the red trace).

For low applied voltage, we see two peaks: the main EIT peak at $\Delta = 0$ MHz and another at $\Delta = -75.63$ MHz, which corresponds to the hyperfine structure transition $5P_{3/2}(F = 3) \rightarrow 40S_{1/2}$. Since the coupling laser is scanned, the separation between these two peaks is the adjusted hyperfine splitting determined by accounting for the Doppler mismatch between the probe and coupling lasers with $120.96((\lambda_p/\lambda_c) -1)$ MHz, see Ref. 53. Here, λ_p and λ_c are the wavelengths of the probe and coupling lasers, and 120.96 MHz is the hyperfine structure separation between $5P_{3/2}(F = 3)$ and $5P_{3/2}(F = 4)$.[51,52,54–56,58] The separation of the two EIT features allows us to accurately calibrate the coupling laser detuning.

Figure 5 shows EIT signals for various applied voltages. This series of EIT signals allows us to observe several interesting features. In addition to Stark shifts and line broadening, we see other features that appear in the EIT lines at higher applied voltages. For sufficiently large applied voltages, the $nS_{1/2}$ levels are crossed by higher-lying, higher-polarizability Rydberg states. For example, the first of these energy level crossings (ELCs) is with the $(n - 3)F_J$ states at approximately 5.5 kV/m, 700 V/m, and 290 V/m for $28S_{1/2}$, $40S_{1/2}$, and $47S_{1/2}$, respectively. This provides a secondary check of our fit to theory, as it provides recognizable features at predicted E-fields, independent of our laser frequency calibration. Figure 6 shows a close-up of the first two ELCs of the $28S_{1/2}$ state, more on this point is discussed below.

The structures in Fig. 5 stem from two sources. First, these structures are due to the ELC beginning to appear in the spectra. Second, the source of these structures (that eventually develop into double peaks for higher voltages) is a result of inhomogeneities in the field
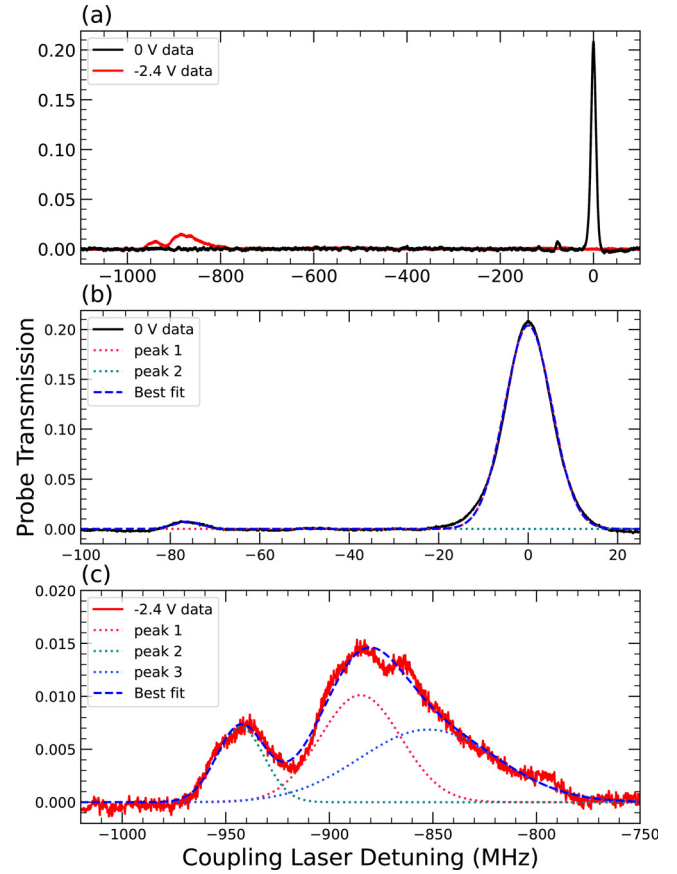

FIG. 4. Plot of probe EIT transmission relative to the probe absorption plotted against the coupling laser detuning (Δ). (a) The black-solid curve is the transmission trace for the 40S Rydberg state when no voltage is applied across the plates. The red-dashed curve is the transmission trace for the 40S Rydberg state when a potential of -2.4 V is placed on the plates. (b) and (c) Close-up of the 0 and -2.4 V traces, respectively. The individual Gaussian fits are depicted as dotted lines, and there sum showing the best fit is depicted as a dashed line.

across the laser beam propagation path. The inhomogeneities in the field are mainly caused by (1) non-parallel plates, (2) imperfections in the surface of the electrodes due to attaching a lead to the plates [as our current plates have a dimple (and discontinuities) in the very center where the leads are mounted], and (3) fringing fields at the edge of the plates.

The EIT signals broaden with applied voltage as seen in Fig. 5. This broadening is likely due to a non-uniform field across the plates along the laser propagation path. Furthermore, additional broadening may be present from local charge distributions. These are likely from ionization of the Rydberg atoms through collisions.[38] Additionally, these E-field inhomogeneities are amplified by the fact that the Stark effect is quadratic for nondegenerate energy levels.[41] Imperfect plate geometries have other ramifications as we discuss in Sec. IV B.

The Stark shift Δ is determined by fitting the trace to two to four Gaussian profiles using non-linear least-squares minimization, with fit parameter uncertainties determined by inverting the Hessian matrix
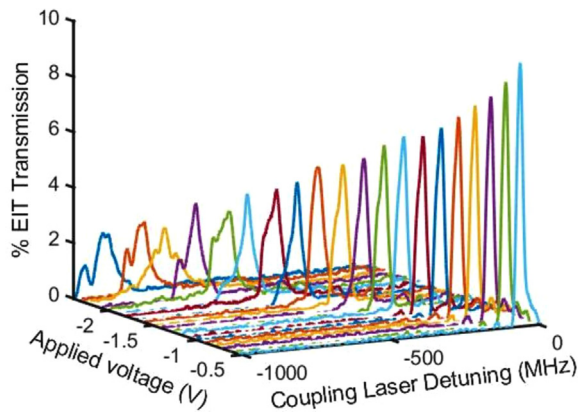
FIG. 5. EIT signals (for scanning the coupling laser) showing Stark shifts for various applied voltages for $40S_{1/2}$.

representing the fit quality second derivative. A voltage uncertainty due to scope jitter and thermal noise of around 1 mV was assumed and held constant in all fittings. The shift from zero fields of the largest amplitude peak is taken to be the Stark shift. Other EIT peaks are present due to the $5P_{3/2}$ hyperfine interval and ELCs. The Gaussian width of these peaks is constrained to equal that of the largest amplitude peak. An additional peak with relaxed width constraints is included at moderate to high voltages to account for broadening and lineshape asymmetry due to geometric imperfections. After fitting a trace to models with two to four peaks, we choose the fit with the minimum number of peaks such that the reduced $\chi^2 < 1.5$.

Shown in Figs. 4(b) and 4(c) are examples of fits for the cases of 0 and -2.4 V applied to the $40S_{1/2}$ state, respectively. For the 0 V case, a two Gaussian model describes the data well and the uncertainty in the Stark shift is $\delta\Delta < 10$ kHz. The -2.4 V fit (4c) required three peaks
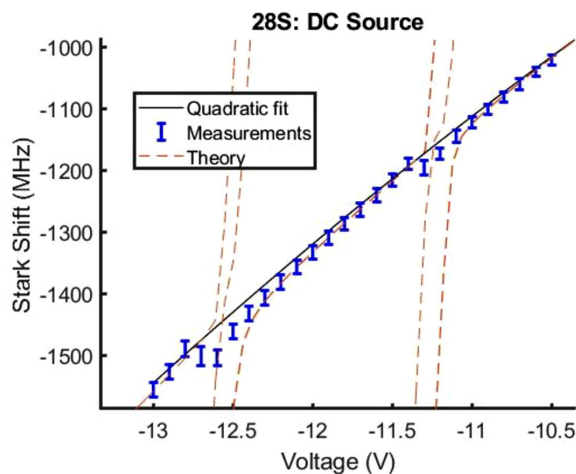

FIG. 6. Expanded view of the ELCs for the $28 S_{1/2}$ state. We can observe the measurement (blue error bars) deviations from the quadratic nature (solid black line) of the dc Stark effect at these locations. Also shown is the theory (red dashed line) that accounts for the ELCs and matched the data much better.

and represents the worst case with a center fit uncertainty of about 200 kHz.

Despite a fit uncertainty of typically $\delta\Delta = 100$ kHz, repeated measurements were found to have a much larger standard error in the Stark shift of typically $\delta\Delta = 5$ MHz. We believe that this is indicative of and consistent with the magnitude of uncompensated systematic errors discussed in Sec. V. Ultimately, the uncertainty $\delta\Delta$ is estimated by the standard deviation from six measurements, as the fit uncertainty is always one to two orders of magnitude smaller than the measurement repeatability. The measured Stark shifts as a function of applied voltage for the Rb $28S_{1/2}$, $40S_{1/2}$, and $47S_{1/2}$ Rydberg states are plotted in Fig. 7. We compare the experimental data in Fig. 7 to the Stark shift calculated by diagonalizing the Hamiltonian in Eq. (1) as a function of applied field E.

A quadratic fit is also shown for reference to the low-field estimate of Eq. (3),

$$\Delta = \frac{1}{C_{cal}^2}(V - V_o)^2, \qquad (9)$$

where V_o a voltage offset that was found to persist even after grounding both plates. An offset voltage could occur due to impurities in the metal causing a build-up of charge which cannot be removed, ionization caused by the 480 nm coupling laser, or a galvanic potential. We found the voltage offset is 235 ± 6 mV for this cell. The error stated is from the comparison of the offset for different Rydberg states used. While simply switching the state does not introduce this error, moving the cell in and out of the beam path does since there are inhomogeneities in the plates. A detailed discussion on the plate inhomogeneities follows in Sec. IV B. For each given Rydberg state, we obtained six sets of measurements over the course of two hours that resulted in no notable shift in the voltage offset. For a fixed cell where the beams will be stationary, we can quote a substantially lower uncertainty in the voltage offset. The fits were within a 95% confidence interval. The fit also determines the calibration factor C_{cal} for the cell and Rydberg state, given in Table II. In determining the calibration factor C_{cal}, care must be taken to ensure that the ELCs do not influence its value. The effect of the ELCs is discussed in Secs. IV A and IV B.

A. Energy level crossings

The measured data in Fig. 7 were corrected for the voltage offset and compared to theoretical calculations for the Stark shift. The theoretical Stark maps were obtained by using the Alkali Rydberg Calculator Python package.[42] These comparisons are shown in Fig. 7, where the theoretical model accounts for ELCs from nearby Rydberg states. We show plots for the Stark shift as a function of applied V. In the theoretical curves, the E field was determined using $E = V/d$ (where we use $d = 2.19$ mm). We can see a good consensus between the experimental data and the theoretical model. In particular, on closer inspection, the locations of the ELCs can be seen in the measured data. This is further illustrated in Fig. 6, where we show an expanded view of the ELC for the $28 S_{1/2}$ state spectra, shown in Fig. 7(a). In this figure, the level crossings are easily seen as splitting in the spectra around -11.2 and -12.5 V. On this note, the Stark shifts corresponding to the ELCs can be used to find the calibration factor as well.
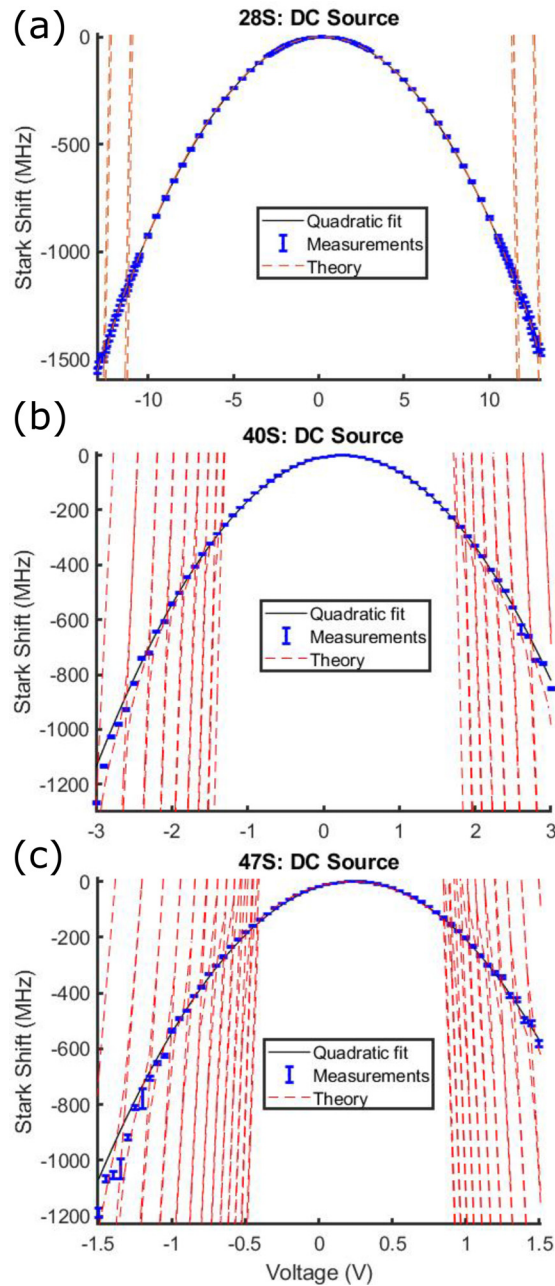
Fig. 7. (a)–(c) correspond to the measured Stark shift for 28S, 40S, and 47S Rydberg states with a dc source (blue errorbars). Also shown are the curve fits using the calibration factor found by Eq. (9). The dashed-red lines are from theory and when these lines become vertical, they indicate the position of the ELCs.

TABLE II. Experimentally obtained calibration constants. The uncertainty is the standard deviation of the calibration constant obtained from the six sets of data. Also shown is the plate separation obtained for C_{cal} and the calculated polarizabilities.

Calibration factors and plate separation		
Rydberg state	C_{Cal} (V/$\sqrt{\text{Hz}}$)	Plate separation (mm)
$28S_{1/2}$ cell 1	$(339 \pm 2.7) \times 10^{-6}$	2.19 ± 0.018
$40S_{1/2}$ cell 1	$(96.7 \pm 0.2) \times 10^{-6}$	2.22 ± 0.005
$47S_{1/2}$ cell 1	$(53.8 \pm 0.3) \times 10^{-6}$	2.18 ± 0.012

state, it would be best to avoid voltage levels where the first ELCs appear. For example, this occurs at approximately 12, 1.5, and 0.6 V for $28S_{1/2}$, $40S_{1/2}$, and $47S_{1/2}$, respectively. The quadratic behavior depicted in Eqs. (3) and (6) fails near the ELCs. As such, using Eq. (7) and measured Stark shifts will need to be limited to voltages well below the first ELC. Thus, for large voltage measurements, Rydberg states with low n should be used, while for small voltages Rydberg states with high n are more suitable (due to the higher sensitivity to weak fields for high n). Alternatively, choosing the electrode plate separation, or manufacturing a variety of plate separations in a cell (with care and attention to fringing fields and geometrical accuracy) allows a given voltage to produce a field appropriate for the accurate measurement by a particular Rydberg state n.

B. Subtleties to calibration

In practice, a calibration must account for or correct three non-idealities: non-uniformity (spatial regions where the electric field between electrodes departs from the relationship $E = V/d$, from fringing fields or imperfections in plate manufacturing), spectroscopic features due to ELC interference (or "line pulling"), and a voltage offset caused by stray charge accumulation, galvanic potentials, or other stray electric field sources. We discuss each of these below.

The fringing fields at the edge of the plate can cause a broadening of the EIT line. Figure 8 shows the EIT signal for the $28S_{1/2}$ with an applied voltage of 0.3 V as the optical beams are moved from the center of the plates ($x = 7.6$ mm) to the edge of the plates ($x = 0$ mm). Recall the optical beams are propagating along the long dimension of the plates. In this figure, we see the EIT signal becomes broader as the beams approach the edge of the plate and we see that the EIT line shape begins to change. Such effects are due to E-field inhomogeneity in the region near the edge where the fringing fields are present (in this case the beams are approaching two sharp corners of the plates). The angle of the cell relative to the incident angle of the beam will play a large role in the broadening as well. With that said, such effects can be accounted for in a calibration. In such calibrations, one needs to be careful when double peaks appear. These double peaks can be the result of imperfections in plate manufacturing.

In the case of the ELCs, we analyze their effect on the fit of Eq. (9). Ideally, the quadratic Stark effect should fit the data well, but the ELCs introduce higher order terms. This can introduce errors in the fit of the data used to find the calibration constant C_{cal}. Therefore, we analyzed how the calibration factors and fits change if we included different voltage ranges (max voltage-min voltage, centered at 0 V) during the fitting process. Figure 9 shows the difference between the data
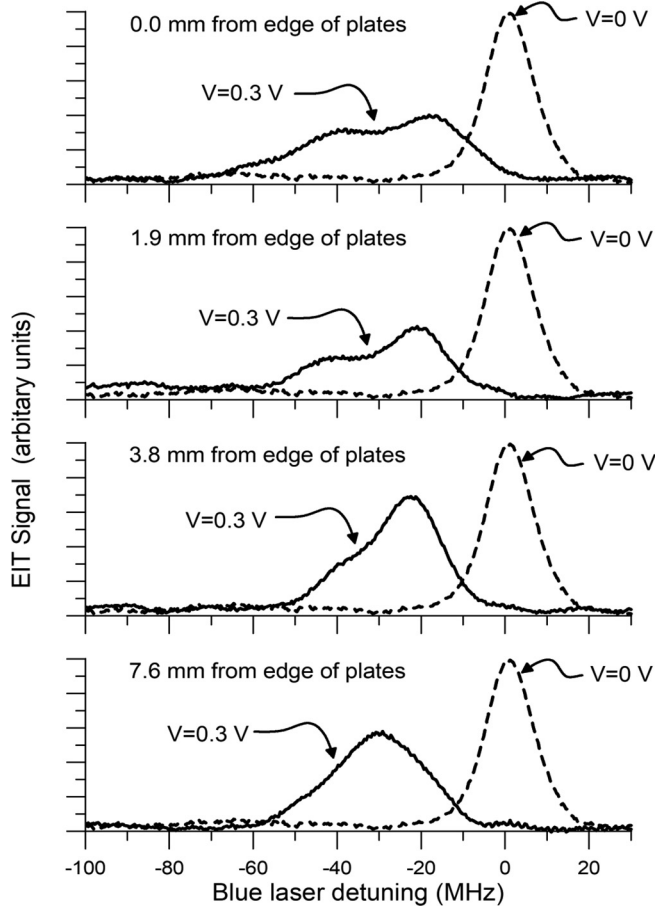
FIG. 8. EIT signal as the optical beams approach the edge of the plate. The plate has a width of 18 mm, the edge of the plate is defined at $x = 0$ mm and the center of the plate is at 9 mm from the edge.

and the fit [i.e., Eq. (9)] for different voltage ranges given by the separate traces. Figure 9(a) shows the difference (i.e., residuals), Fig. 9(b) shows the studentized residuals (|residual|/standard deviation), and Fig. 9(c) shows the calibration factors obtained from the fits for different voltage ranges. Here, we plot the percent difference between the data and the fit for cases where we include different voltage ranges for the different fit traces for the $28S_{1/2}$ state. Note that the large deviations for <2 V in Fig. 9(b) are a result of the smaller error for the smaller voltages applied. This is due in part to the increase in width of the EIT peak as a voltage is increased. For smaller voltages, the standard deviation was less than 1 mV for the peaks with smaller widths, leading to increased fluctuations. It can be seen that the fit with the least deviation is for the case where we use voltages from −9 to 9 V, corresponding to a range of 18 V. In any other case, the fit breaks from the data very quickly. The fits shown in Fig. 7 and the calibration factor C_{cal} given above were obtained by optimizing the voltage range in this manner.

Also shown in Fig. 9(b) are the effects of the ELCs which result in a higher order dependence and do not simply follow the quadratic Stark effect. This is further demonstrated in Fig. 9(c), where we see

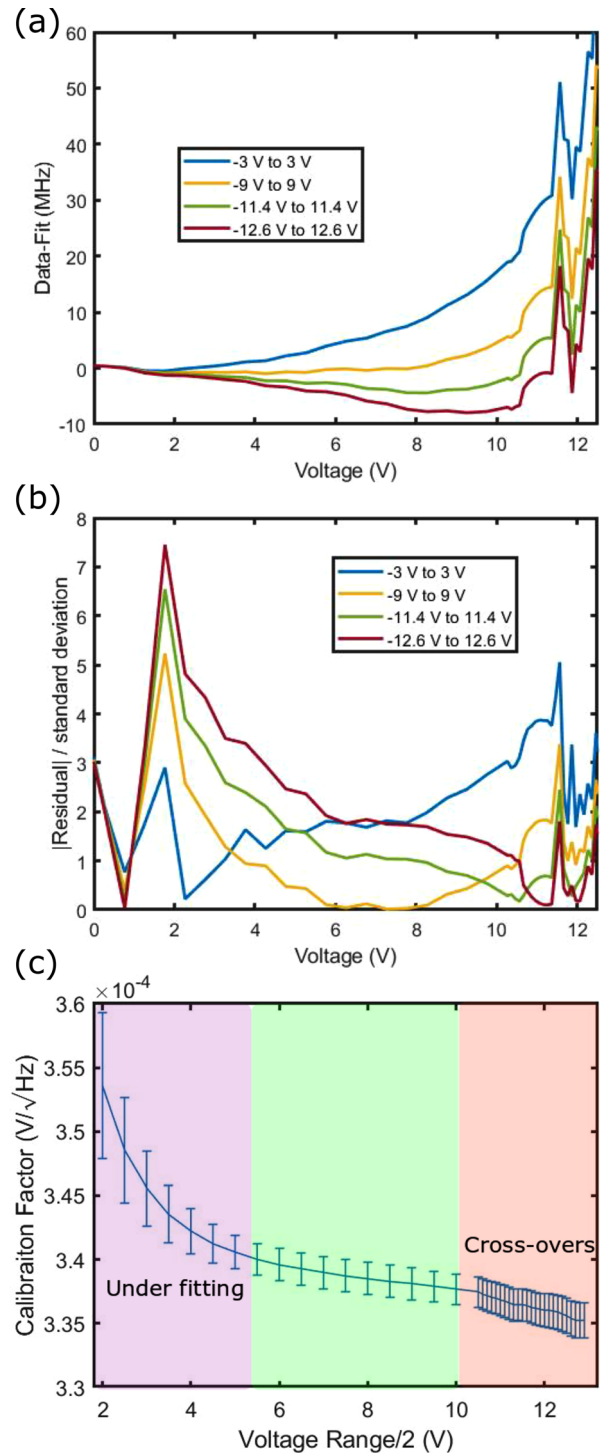
FIG. 9. (a) Difference (residuals) between the experimental data and the fit in Fig. 7. (b) Studentized residuals from (a). Each trace is for a fit incorporating data from the negative voltage out to the positive voltage, as labeled. (c) The calibration factor obtained from fits using different voltage ranges plotted against half the voltage range. These data are for the 28S Rydberg state.

how the calibration factor changes for the different voltage ranges used in the fit. As expected, we see under fitting if not enough data is used (magenta region), a nearly flat line with-in error for the region of good fit (green region), and then a skew of the slope as the voltage range is increased into the region of the ELCs (red region). To overcome the effects of the ELCs at higher voltages, we can use a more precise model to account for their effects, as shown in Fig. 7. The other option is to tune to different Rydberg states to tune the sensitivity or adjust the plate separation. The latter requires the use of several different cells manufactured for specific operating conditions. By tuning the plates, we change the necessary voltage to produce a given electric field.

In the case of the voltage offset, we found that a potential cause is the combination of fringing fields and the charge density present on the plates. As our parallel plates are not infinite, there are contributions that arise from edge effects. These effects have a particularly strong response if the cell is translated horizontally, as shown in Fig. 10. In this case, we mean perpendicular to the optical beams and parallel to the plates. As the cell position is moved so that the optical beams are at the edge of the plates (0 mm trace in Fig. 10), we observe that the voltage offset decreases.

While the positioning of the cell changes the voltage offset, it does not change the shape of the curve. With the exception of the beam position at the very edge of the cell, the calibration factor changed by less than 2% for the other measurements, as shown in the legend of Fig. 10. Thus, long as the calibration curve is acquired and the voltage offset is accounted for, this method has potential as a standard of measurement. However, at the edge of the cell, there is increased uncertainty in the measurement.

Finally, non-uniform plate separation can be an issue for these Rydberg atom sensors. One remedy is to use a microfabricated cell[60] to insure plate uniformity, where microfabrication of a vapor cell allows for better control of the plate or electrode separation as described in Ref. 61.
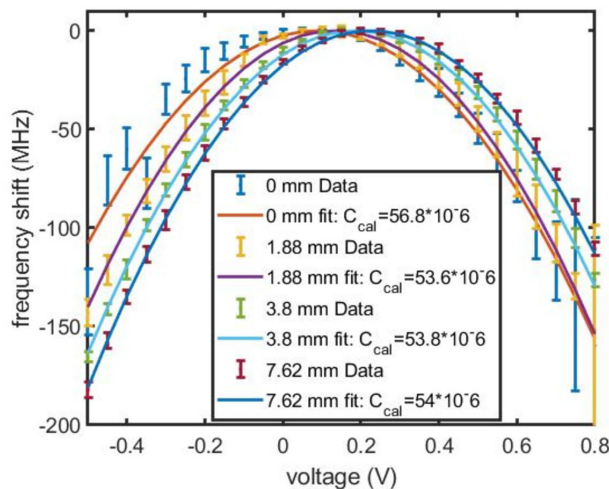

FIG. 10. Stark shift measurements for different horizontal beam positions parallel to the plates shown by the error bars. Also shown is the fit of the data and the extracted C_{cal} factors in the legend. The edge of the cell is at 0 mm, and 7.62 mm is near the center of the cell.

V. UNCERTAINTIES AND ERROR BUDGET

Table III presents an uncertainty budget for our realization of a Rydberg atom-based voltage standard. The measurement uncertainty is limited by a number of systematic effects, which we detail below. Chief among the uncertainties are geometric effects including fringing fields near the perimeter of the plates and plate non-parallelism. These geometric effects systematically influence the relation between an applied voltage and the electric field between the parallel plate electrodes. The nominal relation in Eq. (5) is only strictly valid for infinite parallel plates; the plates in our cell are neither infinite nor parallel. By fitting the Stark shift as a function of applied voltage, we are, in fact, determining an effective scale factor d_{eff} to determine the applied V. The level of agreement between the value of d_{eff} and the physical plate separation d is then a measure of the validity of Eq. (5). We demonstrate a method to measure voltages up to around 10 V with an uncertainty of $\delta V/V = 1.2$ % (with coverage factor $k = 2$, assuming all uncertainties are uncorrelated with normal distributions).

A. Statistical uncertainty

The experimental data are first fit to a multiple Gaussian peak model in order to extract the Stark shift Δ, as discussed in Sec. IV. Typical fit uncertainties are $\delta\Delta = 100$ kHz. The experimental Stark shifts are then fit to the theoretical Stark shifts by taking the minimum χ^2 estimate, with plate separation d and a dc offset voltage V_0 as free parameters. Typical statistical uncertainties are $\delta d = 10^{-6}$ m and $\delta V_0 = 300\,\mu$V. Using Eq. (3), the statistical uncertainty on the voltage measurement is, therefore, approximately

$$\left(\frac{\delta V}{V}\right)^2 = \left(\frac{\delta d}{d}\right)^2 + \left(\frac{\delta V_0}{V_0}\right)^2 + \left(\frac{\delta\Delta}{2\cdot\Delta}\right)^2. \quad (10)$$

For all voltages explored here ($|V|\lesssim 13$ V), $\delta\Delta$ can be made negligible compared to other statistical uncertainties through averaging. We routinely obtain fractional statistical uncertainty in our voltage measurements of $\delta V/V < 0.1$ % from an average of around ten measurements, and our total measurement uncertainty stems from the systematic effects described in the following discussion. For example, with an applied voltage of $V = 1$ V, we achieve a typical statistical uncertainty of $\delta V = 1.4$ mV, limited primarily by uncertainty in the voltage offset V_0. However, due to the quadratic dependence on the field of the Stark shift, for small voltages, the resolution may be limited

TABLE III. Systematic error budget for the voltage measurement. The total uncertainty is taken to be twice the quadrature sum of all contributions.

Uncertainty	$\delta V/V$ (%)
Statistical	0.1
Theory	0.01
Fringe fields	0.4
Laser-plate alignment	0.4
Plate parallelism	0.1
Thermal expansion	<0.01
Magnetic field	<0.01
Total ($k = 2$)	1.2

by fit uncertainty, and additional averaging may be required. Equation (6) indicates that for $\delta\Delta = 100$ kHz, the minimum detectable voltage is roughly 150, 43, and 24 mV for the $n = 28, 40$, and 47 states, respectively.

As stated above, while the fit uncertainty of typically $\delta\Delta = 100$ kHz, repeated measurements were found to have a much larger standard error in the Stark shift of about $\delta\Delta = 5$ MHz.

B. Theoretical uncertainty

Several measurements[47,48,62,63] and calculations[43,64] have been performed of Rb Rydberg state polarizabilities (and related quantities such as lifetimes and quantum defects). For the principal quantum numbers $n = 28$ to 47 considered here, state-of-the-art polarizability calculations have an estimated fractional uncertainty of $\delta\alpha/\alpha \approx 1\%$. However, as stated above, our deviations from theory in α are indistinguishable from an altered fit value of the plate separation d_{eff} in our voltage measurement. Diagonalizing the effective Hamiltonian in Eq. (1), the Stark shift Eq. (3) has additional terms proportional to higher, even powers of E (i.e., E^4, E^6, …), which can become important in high fields, especially near ELCs. Restricting our attention to voltages below the ELCs, inaccuracies in the atomic structure theory can, in principle, cause detectable deviations in the quartic Stark shift terms at a level of $(\delta\alpha/\alpha)^2 \approx 10^{-4}$.

C. Fringe fields

Due to finite plate size, the E-field magnitude is reduced toward the edge of the plates. In our experimental geometry with counter-propagating probes and coupling lasers, this introduces a broadening that increases with increasing applied voltage. The broadening is evident in the EIT traces as a function of applied voltage in Fig. 5. Fringe fields also produce an asymmetric line shape, skewed toward lower magnitude shifts.

A related effect is a residual, roughly unshifted EIT peak due to the atoms which interact with the lasers in the 2.5 mm-long gaps between the field plates and the vapor cell windows. In a simple two-dimensional model of parallel plates with length L and separation d, the electric field along the symmetry axis y may be modeled as

$$E(y) = \frac{V}{\pi d}\left[\arctan\left(\frac{L-2y}{d}\right) + \arctan\left(\frac{L+2y}{d}\right)\right]. \quad (11)$$

However, in comparison with the data, we found that the model of Eq. (11) typically overestimates the size of the unshifted peak by roughly an order of magnitude. This is because Eq. (11) does not capture the effects of 1 mm plate thickness on the gap regions. A finite element simulation of the electric field generated by the plates was found to fully capture the general features of our Stark EIT spectrum.

In order to estimate the effect of the fringe field on the voltage measurement, we simulated the Stark shift spectrum produced by various approximations of plate geometry and comparing to an ideal, constant field $E(y) = E(0)$. Including a two Gaussian model to account for the gap region, the fit to the spectrum derived from our finite element simulation is observed to shift by at most 0.8%, corresponding to a fractional voltage uncertainty of 0.4%.

D. Laser–plate alignment

The incident angle of the laser beams relative to the plates is observed to affect the EIT linewidth. As an example, Fig. 8 shows the EIT signal for an applied voltage of 0.3 V with the lasers traveling along the long dimension of the plates. As the laser beams are translated from the center of the plates ($x = 7.6$ mm) to the edge of plates ($x = 0$ mm), the effect of field fringing becomes more pronounced. This results in increased broadening and a systematic reduction in the fitted Stark shift Δ. We estimate the laser alignment to be stable to within $\delta x \approx 0.1$ mm. From the observed alignment dependence of the Stark shift, this produces a fractional voltage uncertainty of 0.4%.

E. Plate parallelism

The plate parallelism was measured using a microscope to determine the plate separation at each of the four corners. The corner separations were $2.306(11)$, $2.105(7)$, $2.278(7)$, and $2.103(14)$ mm, where the values in parentheses are the standard uncertainties for ten measurements at each corner. This results in an electric field gradient primarily along the long axis of the plates.

The plate non-parallelism is our largest broadening effect. Because d differs by roughly 10% over the length of the plates, the broadening from this effect is roughly 20% of the observed Stark shift, which reduces the measurement sensitivity. Because the Stark shift is approximately quadratic in an electric field, a linear gradient in the plates produces an asymmetric line shape skewed toward lower magnitude shifts. Simulating the effect of the field gradient on our Gaussian fit results in a maximum shift of 0.1%.

The small gradient of the plate separation along the short axis of the plates is at most $\partial d/\partial x = 10^{-3}$. Again estimating that the laser position is known to be within $\delta x \approx 0.1$ mm, the measured plate gradient produces an additional pointing related uncertainty in the voltage measurement of 8×10^{-5}.

Furthermore, the calibration factor, C_{cal}, can also be used to find the separation of the plates, assuming the $\alpha(0)$ are known. The idea of using Stark shift to determine the plate separation was discussed in Ref. 59. This is done by rearranging Eq. (8) to give

$$d = \sqrt{\frac{\alpha}{2}}\,C_{cal}. \quad (12)$$

Using $\alpha(0)$ and C_{cal} given in Tables I and II, respectively, the estimated plate separation for the different is determined and shown in Table II. We average the d for three different states and we found the plate separation to be 2.19 mm. The value of $d = 2.19$ mm is the same value obtained by average the separation of the four corners for the cell given above.

F. Thermal expansion

The thermal expansion coefficient for stainless steel is typically of order 10^{-5} K^{-1}. Assuming typical laboratory conditions with temperature uncertainty 1 K, this leads to a negligible voltage uncertainty of order $\delta V/V \approx 10^{-5}$. Even for more demanding environments of a deployable sensor where temperature could vary by 10 K or more, thermal effects are expected to be well below other uncertainties.

G. Magnetic field

We estimate the error due to static magnetic fields B typical of a laboratory environment by calculating the Stark shift with and without a 0.1 mT field present. For the Rydberg states considered here, the effect is to systematically reduce $\alpha(0)$ by approximately 1 part in 10^4. We neglect this effect in our analysis as it is approximately an order of magnitude smaller than the theoretical uncertainty in $\alpha(0)$ for most Rydberg states. This uncertainty due to magnetic field could easily be reduced by one to two orders of magnitude by mounting a three-axis magnetoresistor or Hall sensor to the voltage standard vapor cell and including a Zeeman term in the fit Hamiltonian.

VI. AC VOLTAGE MEASUREMENTS

In addition to dc measurements, our measurement scheme may be modified to measure 60 Hz ac voltage by monitoring the periodic, quasi-dc Stark effect. However, 60 Hz ac voltage measurement require different read-out methods. The ac Stark effect would result in a linear shift to the EIT peak, but we instead rely on the slowly changing dc Stark effect in the adiabatic limit where the frequency is slow enough such that the atoms can respond. This limits the measurements to the range of frequencies from dc to 1 MHz; we work with 60 Hz. In this application, we observed that the EIT peak shifts from the 0-voltage location to the peak-voltage location, as expected. Since the calculated polarizability for the dc and ac fields are nearly identical, this peak voltage location also corresponds to the equivalent dc voltage. Thus, by tracking the maximum EIT peak shift, we can make a calibration curve that matches the curve for a dc source, shown in Fig. 11.

For detecting 60 Hz ac voltage, one might consider sweeping a laser fast enough to track the EIT as the 60 Hz source caused it to oscillate from peak-voltage location to zero-voltage location. Unfortunately, such a method requires the laser to scan over a GHz in frequency at a scan frequency much larger than the source bandwidth. Such a scan speed for CW systems results in mode instability and loss in lasing. Here, we demonstrate two methods for determining the peak-to-peak voltage the EIT signal: Stark shift tracking and dc-biased ac voltage sensing.

The first method (Stark shift tracking) relies on similar scans to the ones in the dc voltage measurements. The coupling laser is scanned over a frequency range while 20 traces of the transmission spectrum are gathered. During this time, the EIT peak is oscillating between the 0-voltage location and the peak-voltage location. We take the 20 traces and find the variance at each detuning, shown in Fig. 12. Using these data, we find the maximum shift at the location where the data drops off below a threshold value that lies above the noise. The threshold is when the signal falls to 90% of the peak at the max Stark shift. The extracted drop-off locations are plotted in Fig. 11 for three different states also used for the dc measurements. Also plotted are the dc data to show the agreement in the calibration between the dc data and the ac data taken with this method.

The ac data have increased uncertainty compared to the dc data at the same voltage due to the accuracy of determining the drop-off detuning. As the ac voltage increases, line broadening effects smooth the EIT signal, making a determination of the peak Stark shift increasingly challenging. This issue was mitigated in dc voltage measurements through averaging. Additionally, the voltage-dependent EIT linewidth could potentially result in a voltage-dependent shift in the drop-off
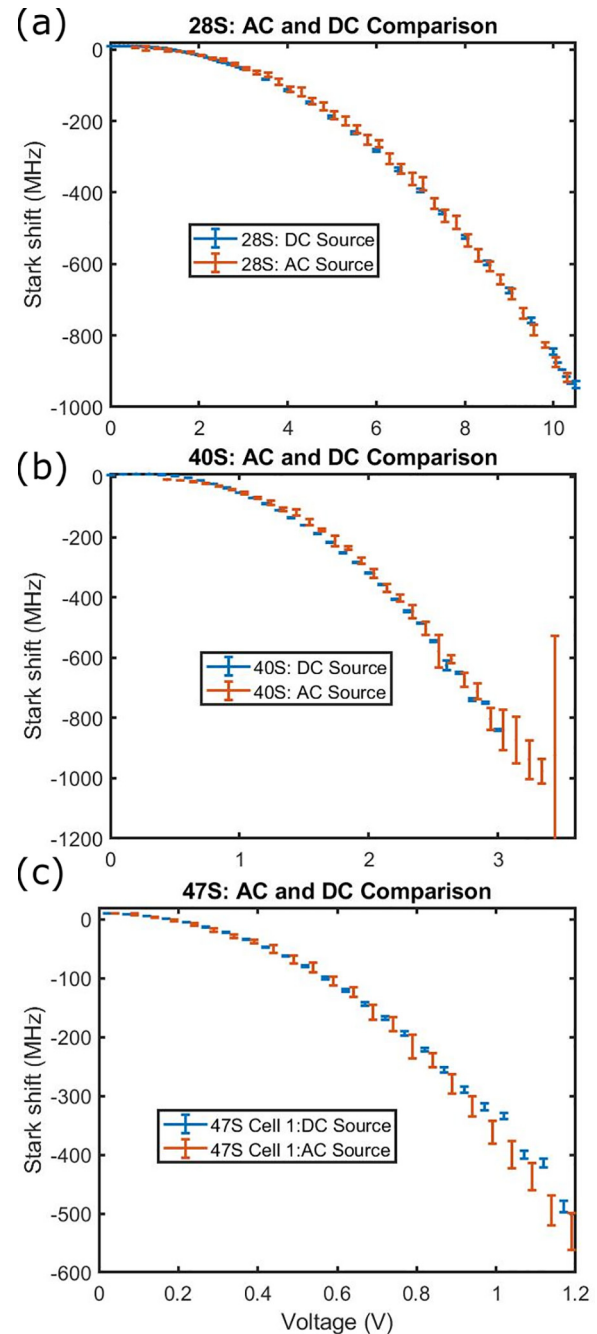

FIG. 11. The Stark shift plotted against the peak voltage of an 60 Hz ac source for the three states 28S (a), 40S (b), and 47S (c). Also included for comparison are the dc experimental data from Figs. 7(a)–7(c).

location. However, this is not apparent here within the bounds of error.

The second method (dc biased ac sensing) relies on the use of a dc calibrated source. As discussed previously, if we have an ac source on the plates, the EIT peak will oscillate between the zero-voltage
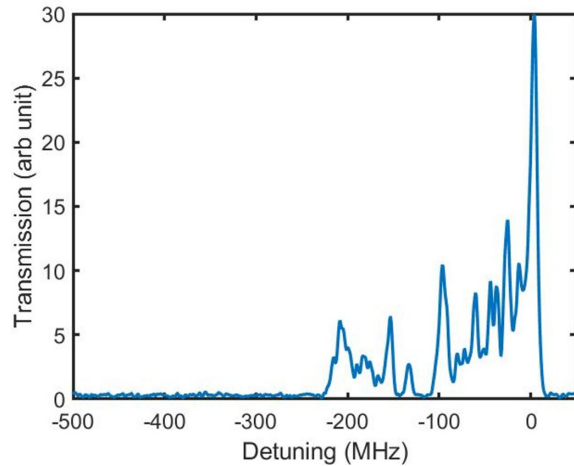
FIG. 12. Sample of mean of 20 traces plotted against the coupling laser detuning for a 1.2 V AC source for the 40S state. As the EIT peak shifts around, the variance increases in the regions where it has passed.

FIG. 13. Sample showing expected EIT transmission (blue) in the presence of a 60 Hz ac field (red) plotted against the phase of the applied ac field. The plots correspond to offset voltages of (a) 0, (b) 0.25, (c) 0.50, and (d) 0.75 V, as labeled.

location and the peak-voltage location. We can observe this shifting if we scan the coupling laser. However, if we lock the coupling laser to the zero-voltage location, we will instead observe transmission only when the ac voltage passes through the zero-voltage location, as shown by the computer generated plot in Fig. 13(a). This produces a transmission peak that we can monitor that is dependent on the ac voltage source. Now, if we apply a calibrated dc voltage along with the ac voltage the transmission peak will shift since the ac voltage at which the voltage sum crosses zero is no longer when the ac voltage passes zero, shown in Figs. 13(b) and 13(c). However, if the dc voltage is increased to a value higher than the peak voltage, the transmission will begin to vanish, as shown in Fig. 13(d).

In this method, we apply a calibrated dc voltage as an offset to an ac voltage source that we wish to determine. We track the height of
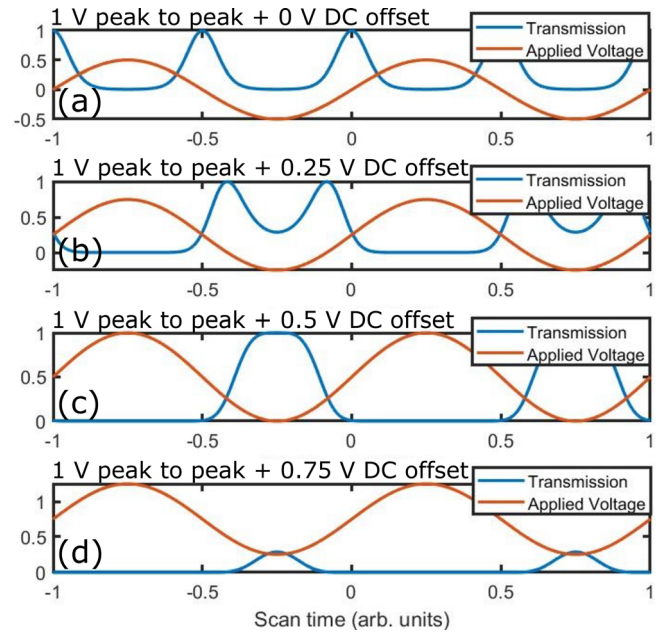
the transmission peaks in Fig. 13. As we scan the dc voltage source from 2 to 2 V, we can see the transmission appear and then vanish, as shown in Fig. 14(a). The voltage difference in the two drop-off locations in the dc voltage scan defines the peak to peak voltage of the applied ac voltage. Figure 14(a) shows the traces of dc voltage scan for several different ac voltages, and Fig. 14(b) shows the extracted peak to peak voltages plotted against the applied voltage.

DC biased ac sensing has certain advantages when compared to Stark shift tracking. In the case of Stark shift tracking, we must average
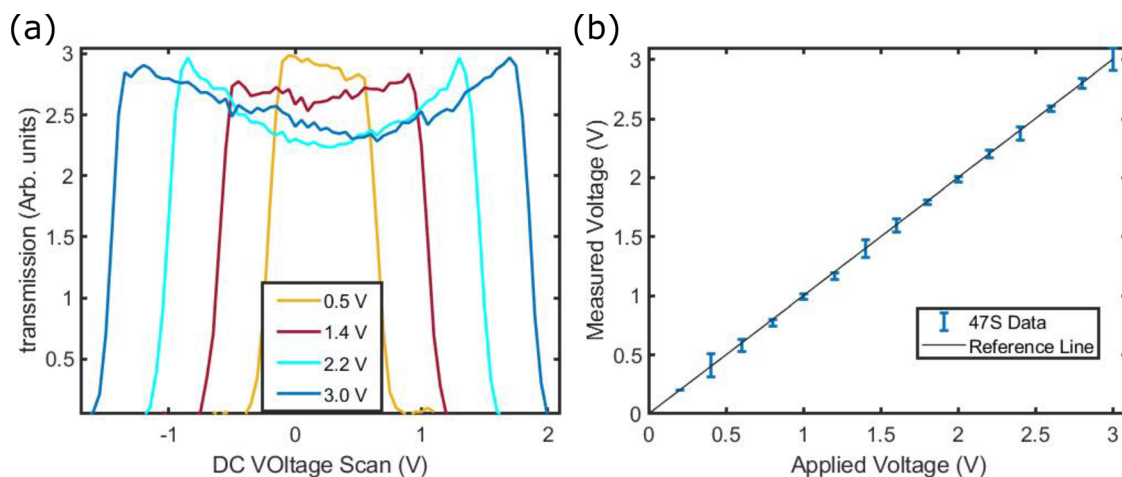

FIG. 14. (a) Sample of traces for different ac voltages where the peak transmission is plotted against the calibrated dc voltage. (b) The width of the traces in (a) that correspond to the peak to peak voltage, plotted against the applied peak to peak voltage (V). These data are for the 47 S state. Black is the one-to-one line as a guide, and blue is the extracted ac voltage.

for a long time to improve the statistics enough to measure larger voltages. However, for dc biased ac sensing, we do not have this same limitation since the measurement occurs at the zero-voltage location with maximum EIT peak height. Unfortunately, the maximum ac voltage we can sense is limited by the range of our calibrated dc source. While this voltage is higher than measurements with the Stark shift tracking method, it is still limited. Furthermore, this method requires a laser lock that is stable to less than 1 MHz for the probe and coupling lasers.

VII. CONCLUSION AND DISCUSSION

In this manuscript, we have demonstrated an alternative voltage standard with 1.2% uncertainty based on Rydberg atoms. This voltage calibration standard is realized through the dc Stark shift of a Rydberg EIT. Additionally, we discuss how the calibration factor C_{cal} can be used to find the plate separation. We also demonstrate two methods to measure 60 Hz ac sources with minimal modification of the apparatus.

We analyzed various sources of uncertainty that arose from non-uniform electric fields due to geometric imperfections. The combination of these effects produce broadened, asymmetric EIT lineshapes, which can be reasonably accounted for through finite element analysis. We also discussed the effects of the ELCs on the EIT spectra. These considerations are key to developing a portable Rydberg standard and will affect the sensitivity, range, and reliability for future atom-based voltage sensors.

In future implementations of a Rydberg atom-based voltage standard, uncertainties arising from geometrical effects could be substantially mitigated by using a three photon excitation scheme.[57] The use of three non-colinear laser beams reduces the overlap volume to roughly $\sim r^3$, where r is the radius of the laser beams. The overlap volume can be placed at the center of the field plates where the E-field is most uniform. Such a scheme would substantially reduce our three largest sources of uncertainty, potentially bringing the total voltage uncertainty below the 0.1% level. The reduced number of atoms participating in the interaction is compensated somewhat by the narrower EIT linewidths ($\sim$100 kHz), though additional averaging would likely be required.

There is room for improvement in plate parallelism as well. For instance, a relative uncertainty in d of 10^{-4} is possible with gauge-block construction[45] or at $<2 \times 10^{-5}$ with interferometric techniques.[36,37] It is also possible to achieve high parallelism in a microfabricated cell.[60,61] The use of similar vapor cells with internal electrodes are currently being investigated for voltage measurements and other applications.[39] However, in this type of cell, care needs to be taken to ensure that any coating placed on the electrodes does not cause shielding of the applied voltage and, in turn, the E-field seen by the atoms.[38]

In conclusion, this study on the dc and 60 Hz ac fields will provide insight for future advancements for the realization of a self-calibrated, low SWAP-C, deployable voltage standard. Future work will include the use of three-photon excitation schemes and vapor cells with more precise plate separation, including microfabricated cells. We emphasize that a future device could, given sufficient accuracy in the polarizability and plate spacing, provide voltage measurements based directly on fundamental constants. In the near future improvements to the EIT resolution, stability and geometrical uncertainties could result in a device with comparable uncertainty to Zener diodes systems.

AUTHOR DECLARATIONS
Conflict of Interest

The authors have no conflicts to disclose.

Author Contributions

Christopher L. Holloway: Conceptualization (equal); Data curation (equal); Formal analysis (equal); Methodology (equal); Supervision (equal); Validation (equal); Writing – original draft (equal); Writing – review and editing (equal). **Nikunjkumar Prajapati:** Data curation (equal); Formal analysis (equal); Methodology (equal); Visualization (equal); Writing – review and editing (equal). **Jeffery A. Sherman:** Methodology (equal); Validation (equal); Writing – review and editing (equal). **Alain Rüfenacht:** Data curation (equal); Methodology (equal); Writing – review and editing (equal). **Alexandra B. Artusio-Glimpse:** Data curation (equal); Methodology (equal); Validation (equal); Visualization (equal); Writing – review and editing (equal). **Matthew T. Simons:** Conceptualization (equal); Data curation (equal); Methodology (equal); Validation (equal); Writing – review and editing (equal). **Amy K. Robinson:** Data curation (equal); Methodology (equal); Validation (equal). **David S. La Mantia:** Formal analysis (equal); Investigation (equal); Methodology (equal); Validation (equal); Visualization (equal). **Eric B. Norrgard:** Formal analysis (equal); Investigation (equal); Methodology (equal); Validation (equal); Visualization (equal); Writing – review and editing (equal).

DATA AVAILABILITY

The data that support the findings of this study are available from the corresponding author upon reasonable request.

REFERENCES

[1] T. F. Gallagher, *Rydberg Atoms* (Cambridge University, Cambridge, 1994).
[2] A. K. Mohapatra, T. R. Jackson, and C. S. Adams, Phys. Rev. Lett. **98**, 113003 (2007).
[3] J. A. Gordon, C. L. Holloway, S. Jefferts, and T. Heavner, "Quantum-based SI traceable electric-field probe," in Proceedings of IEEE International Symposium on Electromagnetic Compatibility, 2010.
[4] J. A. Sedlacek, A. Schwettmann, H. Kubler, R. Low, T. Pfau, and J. P. Shaffer, Nat. Phys. **8**, 819 (2012).
[5] C. L. Holloway, J. A. Gordon, A. Schwarzkopf, D. A. Anderson, S. A. Miller, N. Thaicharoen, and G. Raithel, IEEE Trans. Antenna Propag. **62**(12), 6169 (2014).
[6] C. L. Holloway, M. T. Simons, J. A. Gordon, P. F. Wilson, C. M. Cooke, D. A. Anderson, and G. Raithel, IEEE Trans. Electromagn. Compat. **59**(2), 717 (2017).
[7] S. Kumar, H. Fan, H. Kübler, J. Sheng, and J. P. Shaffer, Sci. Rep. **7**, 42981 (2017).
[8] M. Tanasittikosol, J. D. Pritchard, D. Maxwell, A. Gauguet, K. J. Weatherill, R. M. Potvliege, and C. S. Adams, J. Phys. B **44**, 184020 (2011).
[9] C. L. Holloway, J. A. Gordon, A. Schwarzkopf, D. A. Anderson, S. A. Miller, N. Thaicharoen, and G. Raithel, Appl. Phys. Lett. **104**, 244102 (2014).
[10] J. A. Gordon, C. L. Holloway, A. Schwarzkop, D. A. Anderson, S. Miller, N. Thaicharoen, and G. Raithel, Appl. Phys. Lett. **105**, 024104 (2014).

[11]J. A. Gordon, M. T. Simons, A. H. Haddab, and C. L. Holloway, AIP Adv. **9**, 045030 (2019).

[12]J. A. Sedlacek, A. Schwettmann, H. Kubler, and J. P. Shaffer, Phys. Rev. Lett. **111**, 063001 (2013).

[13]M. T. Simons, A. H. Haddab, J. A. Gordon, and C. L. Holloway, IEEE Access **7**, 164975 (2019).

[14]M. T. Simons, A. H. Haddab, J. A. Gordon, and C. L. Holloway, Appl. Phys. Lett. **114**, 114101 (2019).

[15]M. Jing, Y. Hu, J. Ma, H. Zhang, L. Zhang, L. Xiao, and S. Jia, Nat. Phys. **16**, 911 (2020).

[16]A. B. Artusio-Glimpse, M. T. Simons, N. Prajapati, and C. L. Holloway, IEEE Microwave Mag. **23**(5), 44 (2022).

[17]C. L. Holloway, M. T. Simons, M. D. Kautz, A. H. Haddab, J. A. Gordon, and T. P. Crowley, Appl. Phys. Lett. **113**, 094101 (2018).

[18]D. H. Meyer, P. D. Kunz, and K. C. Cox, Phys. Rev. Appl. **15**, 014053 (2021).

[19]A. Robinson, M. T. Simons, and C. L. Holloway, Appl. Phys. Lett. **118**(11), 114001 (2021).

[20]Z. Song, H. Liu, X. Liu, W. Zhang, H. Zou, J. Zhang, and J. Qu, Opt. Express **27**(6), 8848 (2019).

[21]D. H. Meyer, K. C. Cox, F. K. Fatemi, and P. D. Kunz, Appl. Phys. Lett. **112**, 211108 (2018).

[22]C. L. Holloway, M. T. Simons, A. H. Haddab, J. A. Gordon, and D. Novotny, IEEE Antenna Wireless Propag. Lett. **18**(9), 1853 (2019).

[23]K. C. Cox, D. H. Meyer, F. K. Fatemi, and P. D. Kunz, Phys. Rev. Lett. **121**, 110502 (2018).

[24]C. L. Holloway, M. T. Simons, A. H. Haddab, J. A. Gordon, and S. Voran, "A multi-band Rydberg-atom based receiver: AM/FM stereo reception," in IEEE Antenna and Propogation Magazine, 2021.

[25]D. A. Anderson, R. E. Sapiro, and G. Raithel, "An atomic receiver for AM and FM radio communication," arXiv:1808.08589v1 (2018).

[26]S. Ottoa, M. K. Hunter, N. Kjærgaard, and A. B. Debb, J. Appl. Phys. **129**, 154503 (2021).

[27]C. L. Holloway, M. T. Simons, A. H. Haddab, C. J. Williams, and M. W. Holloway, AIP Adv. **9**(6), 065110 (2019).

[28]N. Prajapati, A. P. Rotunno, S. Berweger, T. Simons, A. B. Artusio-Glimpse, and C. L. Holloway, AIP: Quantum Sens. Technol. **4**, 034401 (2022).

[29]A. Rüfenacht, N. E. Flowers-Jacobs, and S. P. Benz, Metrologia **55**, S152 (2018).

[30]Y. Tang, V. N. Ojha, S. Schlamminger, A. Ruefenacht, C. J. Burroughs, P. D. Dresselhaus, and S. P. Benz, Metrologia **49**, 635 (2012).

[31]P. D. Dresselhaus, S. P. Benz, C. J. Burroughs, N. F. Bergen, and Y. Chong, IEEE Trans. Appl. Supercond. **17**(2), 173 (2007).

[32]T. Yamada, H. Yamamori, H. Sasaki, and A. Shoji, Jpn. J. Appl. Phys. **48**(7R), 076510 (2009).

[33]O. Rest, D. Winzen, S. Bauer, R. Berendes, J. Meisner, T. Thuemmler, S. Wuestling, and C. Weinheimer, Metrologia **56**, 045007 (2019).

[34]T. J. Witt, D. Reymann, and D. Avrons, IEEE. Trans. Instrum. Meas. **44**(2), 226 (1995).

[35]T. J. Witt, IEE Proc.-Sci. Meas. Technol. **149**(6), 305 (2002).

[36]T. Middelmann, S. Falke, C. Lisdat, and U. Sterr, Phys. Rev. Lett. **109**, 263004 (2012).

[37]J. A. Sherman, N. D. Lemke, N. Hinkley, M. Pizzocaro, R. W. Fox, A. D. Ludlow, and C. W. Oates, "High-accuracy measurement of atomic polarizability in an optical lattice clock," Phys. Rev. Lett. **108**, 153002 (2012).

[38]R. Daschner, R. Ritter, H. Kübler, N. Frühauf, E. Kurz, R. Löw, and T. Pfau, Opt. Lett. **37**(12), 2271 (2012).

[39]R. Daschner, H. Kübler, R. Löw, H. Baur, N. Frühauf, and T. Pfau, Appl. Phys. Lett. **105**, 041107 (2014).

[40]M. G. Bason, M. Tanasittlosol, A. Sargsyan, A. K. Mohapatra, D. Sarkisyan, R. M. Potvliege, and C. S. Adams, New J. Phys. **12**, 065015 (2010).

[41]A. Osterwalder and F. Merkt, Phys. Rev. Lett. **82**(9), 1831 (1999).

[42]E. J. Robertson, N. Šibalić, R. M. Potvliege, and M. P. A. Jones, "ARC 3.0: An expanded Python toolbox for atomic physics calculations," arXiv:2007.12016 (2020).

[43]J. Han, Y. Jamil, D. V. L. Norum, P. J. Tanner, and T. F. Gallagher, Phys. Rev. A **74**, 054502 (2006).

[44]V. A. Yerokhin, S. Y. Buhmann, S. Fritzsche, and A. Surzhykov, Phys. Rev. A **94**, 032503 (2016).

[45]J. M. Amini and H. Gould, Phys. Rev. Lett. **91**(15), 153001 (2003).

[46]M. D. Gregoire, I. Hromada, W. F. Holmgren, R. Trubko, and A. D. Cronin, Phys. Rev. A **92**, 052513 (2015).

[47]M. S. O'Sullivan and B. P. Stoicheff, Phys. Rev. A **31**, 2718 (1985).

[48]M. S. O'Sullivan and B. P. Stoicheff, Phys. Rev. A **33**, 1640 (1986).

[49]D. Das and V. Natarajan, J. Phys. B **41**, 035001 (2008).

[50]H. Friedrich, *Theoretical Atomic Physics*, 4th ed. (Springer, New York, 2017).

[51]See D. A. Steck, http://steck.us/alkalidata for "Rubidium 85 D line data, revision 2.1.6" (2013).

[52]M. Newville *et al.* (2014). "LMFIT: Non-linear least-square minimization and curve-fitting for Python," Zenodo. 10.5281/zenodo.11813

[53]L. Ma, "Electromagnetic field sensing with Rydberg atoms in vapor cell," Ph.D. dissertation (University of Michigan, 2021).

[54]M. T. Simons, A. H. Haddab, J. A. Gordon, and C. L. Holloway, "Applications with a Rydberg atom-based radio frequency antenna/receiver," in Proceedings in EMC EUrope, Barcelona, Spain, 2019.

[55]M. T. Simons, M. Kautz, J. A. Gordon, and C. L. Holloway, "Uncertainties in Rydberg atom-based RF E-field measurements," in Proceedings of EMC Europe, Amsterdam, The Netherlands, 2018.

[56]H. Fan, S. Kumar, J. Sheng, J. P. Shaffer, C. L. Holloway, and J. A. Gordon, Phys. Rev. Appl. **4**, 044015 (2015).

[57]J. P. Shaffer and H. Kübler, "A read-out enhancement for microwave electric field sensing with Rydberg atoms," in Proceedings of SPIE Photonics Europe, 2018.

[58]P. R. Berman and V. S. Malinovsky, *Principles of Laser Spectroscopy and Quantum Optics* (Princeton University, Princeton, 2011).

[59]M. G. Bason, "Coherent atom-light interactions in multi-level systems," Ph.D. thesis (Department of Physics, Durham University, 2009).

[60]J. Kitching, E. A. Donley, S. Knappe, M. Hummon, A. T. Dellis, J. Sherman, K. Srinivasan, V. A. Aksyuk, Q. Li *et al.*, J. Phys.: Conf. Ser. **723**, 012056 (2016).

[61]L. A. Liew, S. Knappe, J. Moreland, H. Robinson, L. Hollberg, and J. Kitching, Appl. Phys. Lett. **84**(14), 2694 (2004).

[62]M. Macks, F. Karlewski, H. Hattermann, S. Höckh, F. Jessen, D. Cano, and J. Fortágh, Phys. Rev. A **83**, 052515 (2011).

[63]W. Li, I. Mourachko, M. W. Noel, and T. F. Gallagher, Phys. Rev. A **67**, 052502 (2003).

[64]C. E. Theodosiou, Phys. Rev. A **30**, 2881 (1984).